Microwave control of thermal-magnon spin transport

J. Liu,[1,*] F. Feringa,[1] B. Flebus,[2] L. J. Cornelissen,[1] J. C. Leutenantsmeyer,[1] R. A. Duine,[3,4] and B. J. van Wees[1]

[1]*Physics of Nanodevices, Zernike Institute for Advanced Materials, University of Groningen, Nijenborgh 4, 9747 AG Groningen, The Netherlands*

[2]*Department of Physics and Astronomy, University of California, Los Angeles, California 90095, USA*

[3]*Institute for Theoretical Physics, University of Utrecht, Princetonplein 5, 3584 CC Utrecht, The Netherlands*

[4]*Department of Applied Physics, Einhoven University of Technology, PO Box 513, 5600 MB Eindhoven, The Netherlands*

(Received 8 November 2018; revised manuscript received 17 January 2019; published 19 February 2019)

We observe that an rf microwave field strongly influences the transport of incoherent thermal magnons in yttrium iron garnet. Ferromagnetic resonance in the nonlinear regime suppresses thermal magnon transport by 95%. The transport is also modulated at nonresonant conditions in two cases, both related to the magnon band minimum. Firstly, a strong enhancement of the nonlocal signal appears at a static magnetic field below the resonance condition. This increase only occurs at one field polarity and can be as large as 800%. We attribute this effect to magnon kinetic processes, which give rise to band-minimum magnons and high-energy chiral surface modes. Secondly, the signal increases at a static field above the resonance condition, where the rf frequency coincides with the magnon band minimum. Our study gives insight into the interplay between coherent and incoherent spin dynamics: the rf field modifies the occupation of relevant magnon states and, via kinetic processes, the magnon spin transport.

DOI: 10.1103/PhysRevB.99.054420

I. INTRODUCTION

Thermal magnons are intrinsic fluctuations of the magnetization in a magnet. Nonequilibrium thermal magnons with a small deviation from equilibrium can be described by a temperature and a chemical potential [1]. They can be generated by a temperature gradient, a process known as the spin Seebeck effect (SSE) [2]. Moreover, they can be electrically excited [3–11] and diffusively propagate under a gradient of the magnon chemical potential, $\nabla\mu_{\mathrm{m}}$, with a diffusion length as long as 10 μm at room temperature [5]. These magnons have energy up to $k_{\mathrm{B}}T \sim 6$ THz, where exchange energy dominates. Lately, a lot of effort has been made to control the transport of these electrically excited incoherent high-energy magnons [12–14], because they open up a new way of miniaturizing magnonic devices, due to their short wavelength and their dc-current controllable character. Recently, long-distance electrically controlled propagation has also been realized in an antiferromagnet [15].

In contrast, coherent magnons have well-defined frequency and long wavelength. They can propagate over long distances on the order of centimeters as coherent waves, which is appealing for logic implementation in magnonic devices [16–18]. They can be excited by a microwave field, in a fashion depending on the relative orientations of the rf field ($\mathbf{h}_{\mathrm{rf}}$) and magnetization ($\mathbf{M}$): when $\mathbf{h}_{\mathrm{rf}} \perp \mathbf{M}$, a uniform precession mode, known as ferromagnetic resonance (FMR) [16,17,19], can be excited. For $\mathbf{h}_{\mathrm{rf}} \parallel \mathbf{M}$, parametric pumping [20] can be realized. Generally, for a ferro- or ferrimagnetic insulator, an rf field driving it into FMR oscillates at gigahertz (GHz) frequency, where magnetic dipole interactions dominate. Alternatively, coherent magnons with terahertz (THz) frequency can be excited by femtosecond laser pulses [21,22]. Moreover, spin orbit torque (SOT) can also generate coherently propagating magnons [23].

The dispersive properties of magnons in thermal equilibrium can be described by the dipole-exchange spin wave spectrum [24,25]. Due to their bosonic nature, the distribution obeys Bose-Einstein statistics. The interplay between incoherent thermal magnons and coherent magnons has been under debate for a decade [16,26–29] and its better understanding would also lead to crucial insights into magnon Bose-Einstein condensation (BEC), which has already been observed at room temperature [30].

Here, we study the transport of electrically injected and Joule-heating induced thermal magnons in the presence of an rf field. We find that for an in-plane magnetization, the rf power can have a strong influence on the transport in a few special situations: (i) at the onset of kinetic processes, which give rise to a large population of band-minimum magnons and higher-energy magnons with chiral surface mode character; (ii) at the ferromagnetic resonance (FMR) condition; and (iii) when the rf field oscillates at the frequency of the band-minimum magnons.

II. EXPERIMENTAL SETUP

The devices are fabricated on 210-nm and 100-nm-thick single-crystal yttrium iron garnet (YIG) films. Figure 1(a) shows a schematic of a typical device: two 7-nm-thick Pt strips on YIG are contacted to Ti|Au leads for electrical connection. An on-chip stripline with a shorted end is also made of the Ti|Au layer. The stripline is connected to a vector

*jing.liu@rug.nl

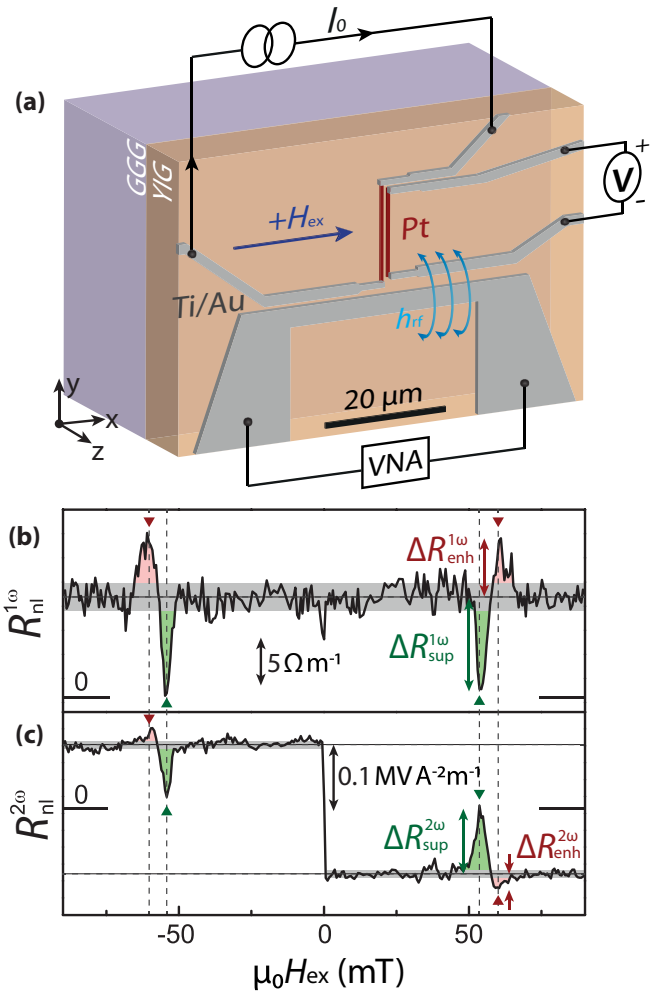

FIG. 1. Experiment schematic and typical results. (a) The YIG film lies in the xy plane on top of GGG substrate. Pt (red) strips are along the y axis. Ti/Au leads (grey) contacted to Pt strips are connected with measurement setups. An ac current with rms value of I_0 is sent through the left Pt strip. Using a lock-in technique, we measured the first and second harmonic voltages by the right Pt strip. The Ti/Au structure on the bottom side is a shorted end of a coplanar stripline where an rf current is driven through by a VNA, resulting in an rf magnetic field $\mathbf{h}_{rf}$. An external magnetic field H_{ex} is applied along the x axis with positive sign corresponding to the positive x direction. Field-dependent (b) first and (c) second harmonic nonlocal resistances. At resonance (green triangles), both first and second harmonic signals are suppressed, indicated by the green areas with magnitudes defined as $\Delta R^{1\omega}_{sup}$ and $\Delta R^{2\omega}_{sup}$. At a higher field (red triangles), there is an enhancement of the signals (red areas) with magnitudes of $\Delta R^{1\omega}_{enh}$ and $\Delta R^{2\omega}_{enh}$. The grey bar represents the baseline resistance with a width corresponding to its standard deviation. The injector-to-detector distance is 1 μm on top of a 210-nm-thick YIG. A continuous rf power is applied: $P_{rf} = +19$ dBm and $\omega_{rf}/2\pi = 3$ GHz.

network analyser (VNA), which sends a high-frequency ac current through the line and generates the rf field $\mathbf{h}_{rf}$, mostly out of the film plane at the Pt device. An external static field H_{ex} is applied to align the magnetization of YIG in the film plane perpendicular to the Pt strips. Devices on 210-nm and 100-nm-thick YIG have injector-to-detector distances of 1 μm and 600 nm, respectively. Details about the sample preparation and experimental setup are given in Ref. [31], S1 and S2, respectively.

To study the transport of thermal magnons, we conduct a nonlocal measurement, where we send an ac current through one of the Pt strips (injector) as shown in Fig. 1(a). This ac current oscillates at a frequency less than 20 Hz, which is quasi-dc comparing with the frequencies of the current through the stripline: 3, 6, and 9 GHz. Via the spin Hall effect (SHE) in Pt, electron spin accumulation at the Pt|YIG interface leads to nonequlibrium magnon spin accumulation. Under a gradient of the magnon chemical potential, magnon spins diffuse towards the other Pt strip (detector), where the reciprocal process takes place, namely magnon electrical detection. Magnon spin current converts back into an electron spin current, which can be measured as an electrical voltage via the inverse spin Hall effect (ISHE). Meanwhile, the Joule heating associated with the current passing through the Pt injector, $\sim I_0^2 R$, induces a thermal gradient in YIG, which drives a magnon spin current both horizontally and vertically [32]. This causes a nonequilibrium magnon accumulation and depletion near the Pt injector and at the bottom of the YIG film, respectively, which both propagate under a gradient of magnon chemical potential. Depending on the ratio of injector-to-detector distance to the YIG thickness, one will dominate. We refer to this process as thermal magnon injection. The resulting nonequilibrium magnon spin current can also be detected by the Pt detector via ISHE. Due to the competition between the magnon spin currents with opposite sign coming from the top and bottom of YIG in the vicinity of the injector, the measured ISHE voltage changes sign as a function of the injector-to-detector distance [32]. The results shown in this paper are all in the regime of large injector-to-detector distance.

With a lock-in technique, we separately study the magnon spin transport resulting from the electrical and thermal injection by measuring the first and second harmonic nonlocal voltages ($V^{1\omega}_{nl}$ and $V^{2\omega}_{nl}$), which are recorded at the same ($\omega_{\text{lock-in}}$) and double frequency ($2\omega_{\text{lock-in}}$) of the excitation current I_0. We define the first and second harmonic nonlocal "resistance" as

$$R^{1\omega}_{nl} = V^{1\omega}_{nl}/(I_0 L), \tag{1}$$

$$R^{2\omega}_{nl} = V^{2\omega}_{nl}/(I_0^2 L), \tag{2}$$

where we not only normalize the nonlocal voltage by the current but also by thelength of the device L, since the ISHE voltage scales with it. We study $R^{1\omega}_{nl}$ and $R^{2\omega}_{nl}$ as a function of the static field H_{ex} in the presence of a continuous rf power, which generates an rf field. We align H_{ex} perpendicular to the Pt strip by eye to achieve the highest magnon injection and detection efficiency. Typical rms-amplitude and frequency of the current are: $I_0 = 200$ μA, $\omega_{\text{lock-in}}/2\pi = 17.777$ Hz. Three different rf frequencies ($\omega_{rf}/2\pi$) are used: 3, 6, and 9 GHz, and applied rf powers (P_{rf}) range from -10 dBm to $+19$ dBm (0 dBm = 1 mW). Moreover, we read the reflected rf power (S_{11} parameter) from VNA to monitor the global magnetization dynamics. The experiments are conducted at room temperature in atmosphere.

III. RESULTS

A. Nonlocal signals under an rf field

In Fig. 1(b), typical field-dependent results show that the first harmonic nonlocal resistance ($R_{nl}^{1\omega}$) has a baseline of $\sim 8\ \Omega\,m^{-1}$ as a result of the magnon injection and detection, while the second harmonic signal ($R_{nl}^{2\omega}$) in Fig. 1(c) reverses its sign by changing the polarity of the magnetization due to the opposite sign of the magnon spins. We define the magnitude of the second harmonic signal as half of the difference between the baseline nonlocal second harmonic resistances at positive and negative static field, which is $\sim 0.1\ MV\,A^{-2}\,m^{-1}$. At FMR, we observe a suppression in both first and second harmonic signals, defined as $\Delta R_{sup}^{1\omega}$ and $\Delta R_{sup}^{2\omega}$. Besides, at a higher field close to the resonance condition there is an enhancement of the signals, denoted as $\Delta R_{enh}^{1\omega}$ and $\Delta R_{enh}^{2\omega}$. To exclude any possible thermal effects that might influence the nonlocal signals at high pumping power, we perform local measurements, where we send the current through one Pt strip and measure the voltage across the same strip (see Ref. [31], S3 and S10). Comparing the local and nonlocal measurements we find that the influence of the rf field on voltages created at the individual injector and detector Pt strips is marginal compared with the influence of the rf field on voltages due to the magnon spin transport. Besides, we confirm that the first harmonic signals scale linearly with the excitation current (see Ref. [31], S7) and are not changed by using different lock-in frequencies for both low and high rf powers. This ensures that the measured nonlocal resistance is due to the magnon spin transport from the electrical magnon injection instead of other spurious effects caused by the microwave power [33].

B. Rf-power dependency

The influence of the rf field on the nonlocal transport strongly depends on the input power to generate the rf field (P_{rf}). In Figs. 2(a) and 4(a), we show typical nonlocal results at different rf powers for rf frequencies of 3 and 6 GHz, respectively. Surprisingly, when the rf power is relatively low, the nonlocal signal changes significantly at a static field lower than the FMR condition. This feature only appears at a positive static field. This should be contrasted with the situation at high powers (above ~ 10 mW), where the suppression and enhancement of the nonlocal signals at the FMR condition and at a higher field than FMR arise for both positive and negative fields: the example in Fig. 1(b) shows the highest-power case. Besides, in the second harmonic signals, we see these asymmetric features, albeit less prominently, which is probably due to the different magnon injection mechanism. In the thermally injected case for the second harmonic signals, the temperature gradient in a thin film complicates the physical scenario [32]. Therefore we focus on the results of the first harmonic signals. We record the magnitude of the asymmetric enhancement at positive static fields as $\Delta R_{asy}^{1\omega}$ as shown in Figs. 2(a) and 4(a), which is plotted against rf power in Fig. 3(e). In the case of 6-GHz rf frequency shown in Fig. 4(a), $\Delta R_{asy}^{1\omega}$ can be more than eight times larger than the baseline resistance of $R_{nl}^{1\omega}$. This asymmetric feature has also been observed with different rf frequencies on YIG with different

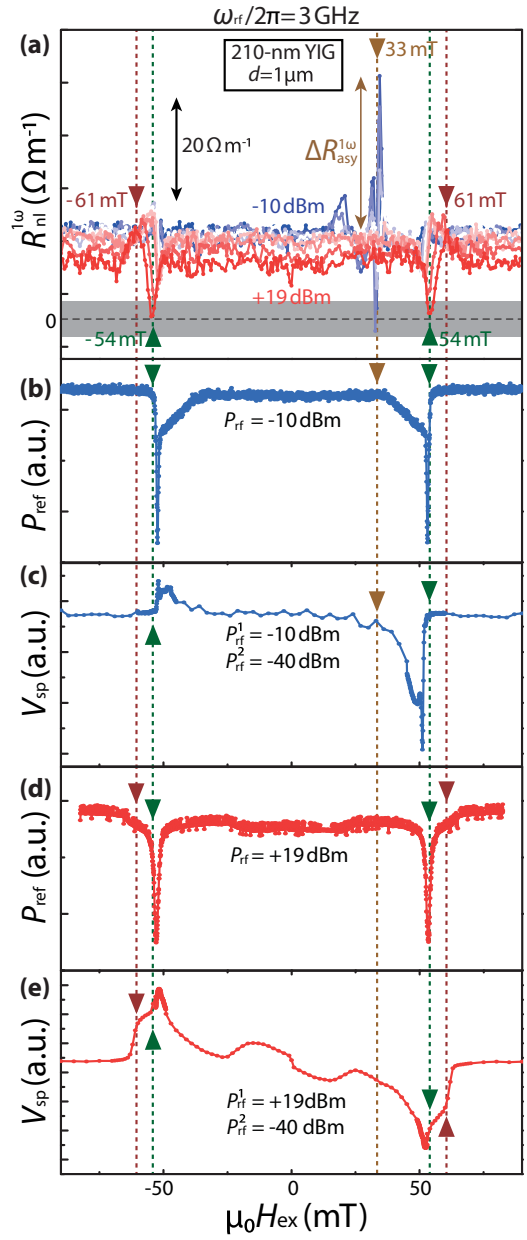

FIG. 2. Comparing nonlocal results with microwave power reflection and spin-pumping measurement. (a) Field dependent first harmonic nonlocal signals at different rf powers. The highest and lowest applied rf powers are −10 (blue) and 19 dBm (red) in (a). The scale bar is 20 $\Omega\,m^{-1}$. The brown, green and red triangles with corresponding vertical dashed lines indicate special field positions. Field-dependent reflected microwave powers at (b) low and (d) high rf power, and spin-pumping ISHE voltage at (c) low and (e) high rf power.

thicknesses. $\Delta R_{asy}^{1\omega}$ increases drastically with rf power until $P_{rf} \sim 10$ mW, where it starts to decrease. Moreover, when we interchange the role of injector and detector, the asymmetric feature changes as shown in Fig. 3(f), whereas the features at FMR ($\Delta R_{sup}^{1\omega}$) and at a higher field than FMR ($\Delta R_{enh}^{1\omega}$) remains almost the same. Besides, comparing results of 210-nm and 100-nm-thick YIG, this asymmetric feature is much more significant in the 210-nm-thick YIG (see Ref. [31], S12).

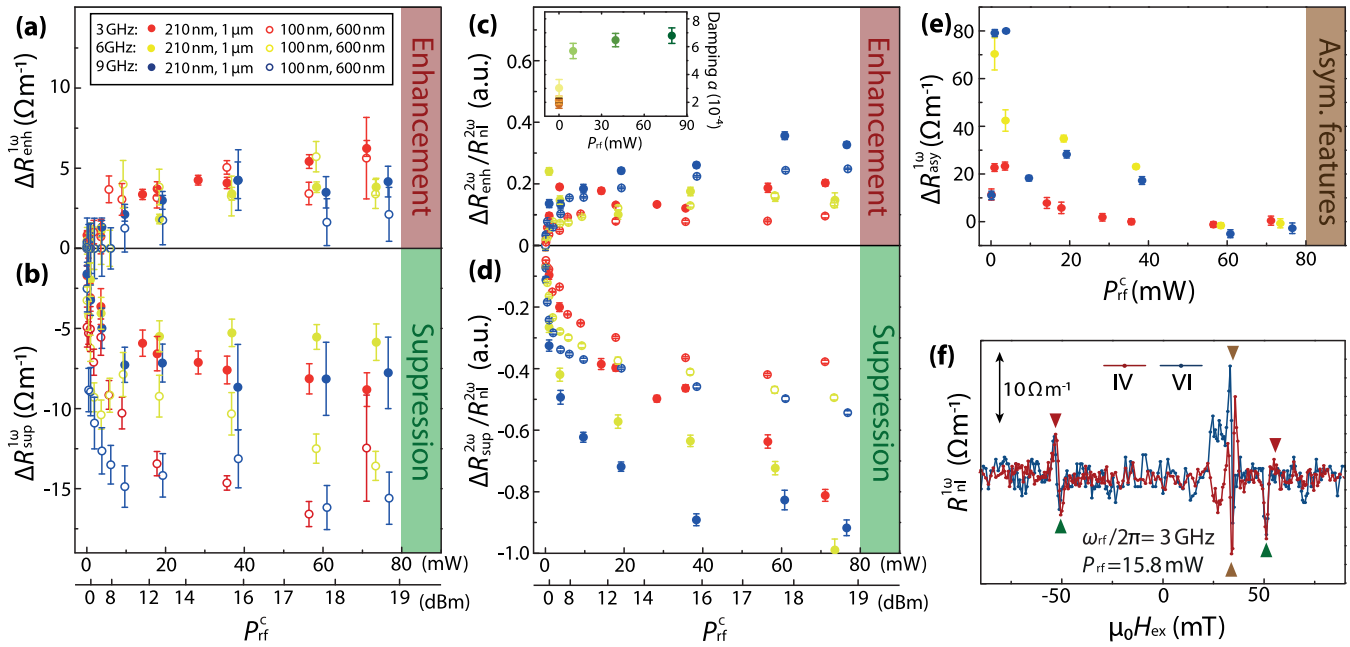

FIG. 3. Suppression and enhancement of nonlocal signals as a function of calibrated rf power. Rf-power dependent (a) $R^{1\omega}_{\rm enh}$, (b) $R^{1\omega}_{\rm sup}$, (c) $R^{2\omega}_{\rm enh}/R^{2\omega}_{\rm nl}$, (d) $R^{2\omega}_{\rm sup}/R^{2\omega}_{\rm nl}$, and (e) $R^{1\omega}_{\rm asy}$ at different rf frequencies (3/6/9 GHz: red/yellow/blue) with different YIG thicknesses (210 nm/100 nm: solid/open dots) and corresponding injector-to-detector distance of 1 μm and 600 nm, respectively. Same color and style code is used for the rf frequency and YIG thickness in (a)–(e). The inset of (c) is the effective Gilbert damping parameter α as a function of $P_{\rm rf}$. Some error bars are smaller than the symbols. (f) The reciprocity check has been performed by interchanging the injector and detector. Two measurement schemes are noted as IV and VI configurations.

We summarize the amplitudes of the suppression and enhancement of the nonlocal signals, $\Delta R^{1\omega}_{\rm sup}$ ($\Delta R^{2\omega}_{\rm sup}$) and $\Delta R^{1\omega}_{\rm enh}$ ($\Delta R^{2\omega}_{\rm enh}$), as a function of the delivered rf power $P^{\rm c}_{\rm rf}$ for different rf frequencies and both YIG thicknesses in Figs. 3(a)–3(d), noting a drastic increase with rf power, until at ∼15 mW there is no significant increase anymore. A similar trend can be seen from the damping parameter of the FMR mode as shown in the inset of Fig. 3(c). Other rf power dependent results (210-nm and 100-nm YIG; 3-GHz and 9-GHz rf frequencies) can be found in Ref. [31], S12, and the data extraction method is provided in Ref. [31], S13. The rf power calibration is provided in Ref. [31], S9. The damping parameters in the inset of Fig. 3(c) are extracted from linear fits of the rf frequency dependent FMR linewidth obtained from the S_{11} measurement (see Ref. [31], S5).

C. Rf-power reflection and spin pumping

We compare the nonlocal results with the microwave reflection and spin-pumping measurement in Fig. 2. The spin-pumping voltage is sensitive to processes near the surface [34], whereas the microwave power reflection is a method to probe the global magnetization. Since spin pumping signal ($V_{\rm sp}$) scales with the length of the Pt strip and in our case it is only 12 μm, we expect $V_{\rm sp}$ to be small. In order to still be able to detect it, we have to use a lock-in technique to modulate between two rf powers or rf frequencies. In Figs. 2(c) and 2(e), we used a low lock-in frequency of 7.777 Hz to modulate between two rf powers of $P^1_{\rm rf}$ and $P^2_{\rm rf}$ with rf frequency of 3 GHz.

At low rf power, when we increase the static field, the reflected microwave power [see Fig. 2(b)] starts to decrease at the static field of $\sim \pm 33$ mT, where we see a prominent change of the nonlocal signal in Fig. 2(a). When the static field reaches ± 54 mT, a sharp dip appears for the reflected rf power with similar amplitude and line shape at both positive and negative static fields, which is a result of microwave power absorption by YIG at FMR. At static fields lower than the resonance condition, the absorption takes place due to the available perpendicular standing spin wave modes [34]. By comparison, the measured spin-pumping voltage changes sign when the static field changes polarity. At low rf power in Fig. 2(c), it also has a big shoulder at fields lower than FMR condition, starting at the static field of ∼33 mT. However, it shows larger amplitude at positive resonance field than that at the negative one.

At high rf power, the reflected microwave power dips at FMR in Fig. 2(d) have larger linewidth, and they do not show the big shoulder at fields lower than FMR condition, compared with the low rf power case. The spin-pumping voltages in Fig. 2(e) show similar amplitudes and line shapes at positive and negative static fields. At lower external fields than FMR, the spin pumping signals can be attributed to the onset of the parametric pumping process. The highly distorted line shape at high rf power is a result of the nonlinear FMR [36,37]. Correspondingly, the nonlocal signals at both positive and negative static field show a suppression at the FMR and an enhancement at a field higher than the FMR. The resonance fields for different rf frequencies and samples are confirmed with the S_{11} and spin-pumping measurements (see Ref. [31], S1 and S2, respectively).

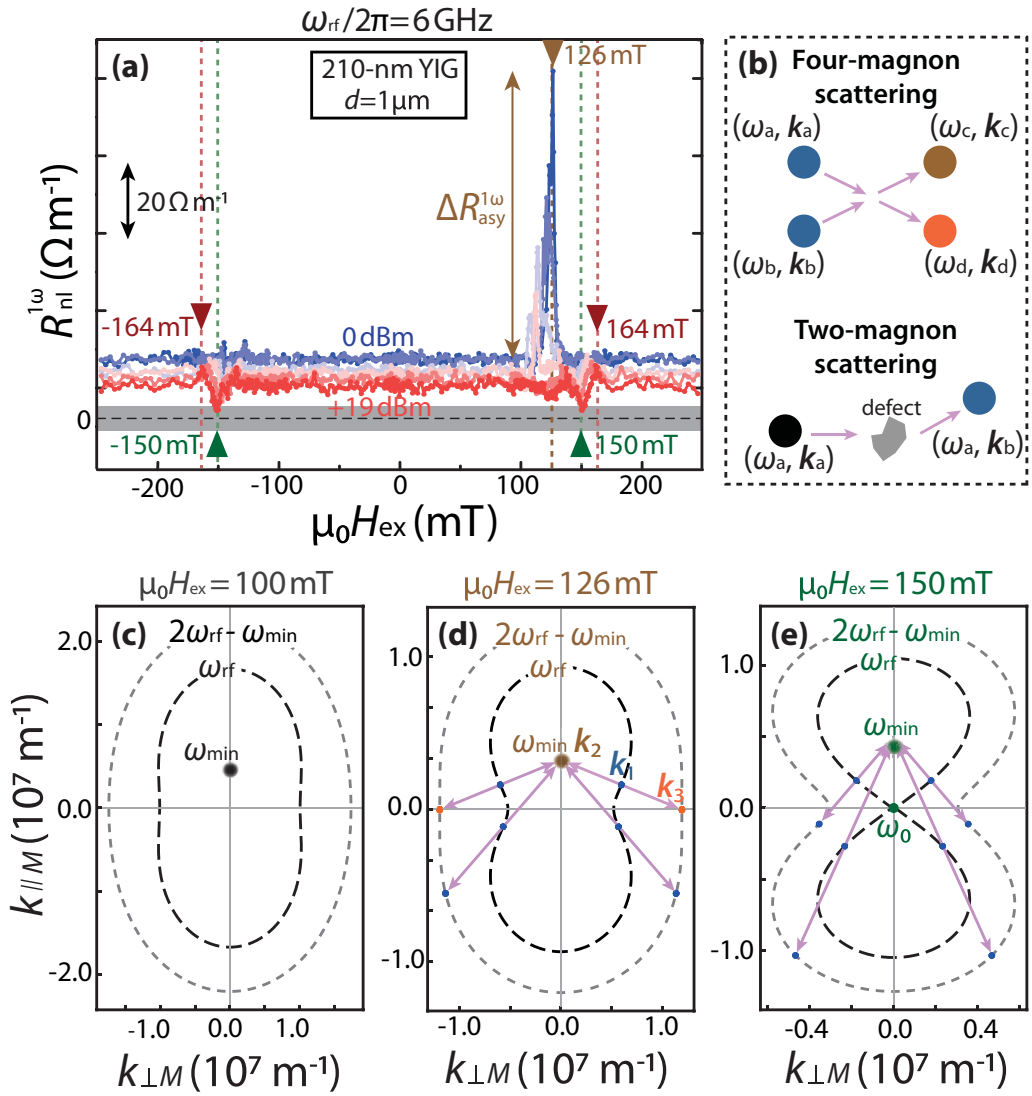

FIG. 4. Comparing nonlocal resistance with relevant iso-frequency curves to illustrate the kinetic process. (a) First harmonic nonlocal results with different applied rf powers, from 0 (blue) to +19 dBm (red). The scale bar is 20 $\Omega\,\mathrm{m}^{-1}$. The brown, green and red triangles with corresponding vertical dashed lines indicate special field values. (b) Magnon scattering processes. Four-magnon scattering: a magnon with frequency of ω_a and momentum of k_a, denoted as (ω_a, k_a), scatter with the other magnon (ω_b, k_b), giving rise to two magnons (ω_c, k_c) and (ω_d, k_d), where energy and momentum are conserved ($\omega_a + \omega_b = \omega_c + \omega_d$, $k_a + k_b = k_c + k_d$). Two-magnon scattering: One incoming magnon (ω_a, k_a) scatters with a defect in the system, resulting in an outcoming magnon (ω_a, k_b), where energy is conserved but momentum is not. [(c)–(e)] Isofrequency curves of 210-nm-thick YIG dispersion relation at static fields of 100, 126, and 150 mT. $k_{\perp M}$ and $k_{\parallel M}$ are wave vectors perpendicular and parallel to the in-plane magnetization, corresponding to the magnetostatic surface mode and backward volume mode. Magnon frequencies of ω_{rf} and $2\omega_{rf} - \omega_{min}$ are in black and gray dashed lines, respectively. $\omega_{rf}/2\pi$ is 6 GHz and ω_{min} is the band minimum at corresponding static field. In (d) and (e), blue dots on the iso-frequency lines of ω_{rf} represent the initial states of the four-magnon scattering. Orange or blue dots on the iso-frequency line of $2\omega_{min} - \omega_{rf}$ represent one of the final states of the four-magnon scattering. The orange one has large $k_{\parallel M}$ component and group velocity in the same direction. Note that the other band-minimum (ω_{min}, $-k_2$) can also be generated due to the similar four-magnon scattering, since the iso-frequency lines are center symmetric with respect to zero-momentum. We draw the lowest magnon dispersion relation with parameters obtained from the Kittel fit of rf power reflection measurement: Gyromagnetic ratio ($\gamma = 27.3$ GHz/T) and saturation magnetization ($\mu_0 M_s = 170$ mT). We used exchange stiffness of 1×10^{-39} J m^2 [35].

IV. DISCUSSION

Inspired by a recent work [38], we compare the first harmonic nonlocal result and the isofrequency lines of the YIG dispersion relation as shown in Fig. 4. We find that at relevant static fields, where the distinct changes of nonlocal resistances appear, various kinetic processes in the magnon cloud are allowed according to energy and momentum conservation. This changes the magnon scattering and the occupation of relevant magnon states so as to alter the transport.

Firstly, at a static field lower than the FMR condition, ~126 mT, we observe a strong increase of $R_{nl}^{1\omega}$ in Fig. 4(a). The applied rf power is relatively low, ~1 mW. At this static field, magnons with frequency of ω_{rf} and momentum

of k_1, denoted as (ω_{rf}, k_1), can efficiently scatter with each other as shown in Fig. 4(d). This results in one magnon at the band minimum (ω_{min}, k_2) and the other with higher frequency ($2\omega_{rf} - \omega_{min}$, k_3), obeying energy and momentum conservation for the four-magnon scattering process ($2k_1 = k_2 + k_3$), as illustrated in Fig. 4(b). The resulting high energy k_3-magnons possess large $k_{\perp M}$ component, which is characteristic of the chiral surface mode [39]. Besides, they have a group velocity pointing in the direction of $k_{\perp M}$. There are various broadening processes, such as two-magnon scattering [see Fig. 4(b)] and phonon-related Gilbert damping, that prepare the magnons with momentum $\mathbf{k}_1$. To compare, we also show the isofrequency lines at 100 mT in Fig. 4(c), where there is no effective kinetic process in the manner described above.

The chiral property of the surface mode excited by the kinetic process might explain why the strong enhancement of nonlocal signals only appears at the positive static field of 126 mT. Moreover, the nonreciprocal property of the surface mode [34,40] manifests itself as shown in Fig. 3(f), where this asymmetric feature is altered upon interchanging the roles of injector and detector. Details can be found in Ref. [31], S8. Besides, the asymmetric feature is much more significant in the 210-nm-thick YIG compared to the 100-nm-thick one (see Ref. [31], S12), because the number of standing spin wave modes increases with increasing film thickness, which enhances the scattering probability [34]. In addition, this corroborates the chiral surface mode origin, because magnetostatic surface modes are better localized at the top and bottom surface in the thicker YIG. Also, $\Delta R^{1\omega}_{asy}$ increases drastically with rf power until ~10 mW, where it starts to decrease. The drastic enhancement of the nonlocal signals might be related with the increasing occupation of the magnon band minimum due to the kinetic process, which significantly facilitates the magnon conduction. Heating due to rf power might be the reason why we do not see this effect at higher rf power [41]. Last but not least, this can also explain the different spin-pumping voltages for the positive and negative static fields at relatively low rf power as shown in Fig. 2(c), because the spin-pumping voltage is sensitive to processes near the surface [34]. Therefore, the secondary magnons with chiral surface mode character contribute to the spin-pumping voltage differently for positive and negative static fields.

Secondly, at a static field corresponding to the FMR condition, ~150 mT, we observe a suppression of the nonlocal signals at relatively large rf power in Fig. 4(a). As shown in Fig. 4(e), the frequency of the FMR mode coincides with the rf frequency ($\omega_{rf} = \omega_0$). Heating due to microwave absorption at FMR opens a bigger precession cone angle and reduces the effective magnetization, which can reduce nonlocal signals (see Ref. [31], S11). However, this can not explain a suppression as large as 95%.

The saturating trend of $\Delta R^{1\omega}_{sup}$ with rf power as shown in Fig. 3(b) is similar to that of the damping parameter in the inset of Fig. 3(c). This suggests a highly nonlinear FMR (NFMR) regime [42–45], where a FMR mode quickly transfers its energy to other degenerate nonzero momentum modes, as indicated by the blue dots on the isofrequency curves of ω_{rf} in Fig. 4(e), which also experience the four-magnon scattering. This process redistributes the energy, which is also known as second-order Suhl spin wave instability [46]. Based on this, one possible reason for the strong suppression of the nonlocal signals at the resonance is that the electrically injected magnons are strongly scattered off by the secondary magnons due to NFMR, but we do not have a full understanding.

Depending on the strength of the rf field, the magnon system reacts differently: With increasing h_{rf}, more magnons are generated, which means a larger deviation from equilibrium. As soon as the deviation surpasses a critical point, the magnon-magnon interaction starts to determine the behavior of the magnon system and the system switches from the linear to the nonlinear regime [27,47,48]. The threshold rf field separating linear and nonlinear regimes is on the order of 0.01 mT for a single-crystal YIG film [43–45,49], which is easily achievable due to the low damping of YIG. The regime of rf field we use is approximately from 0.03 to 1 mT, which is above the threshold rf field. Therefore we observe the influence of the microwave field on nonlocal signals for the in-plane magnetization in the nonlinear regime.

Thirdly, at a static field higher than the FMR condition, ~164 mT, we observe an increase of $R^{1\omega}_{nl}$ in Fig. 4(a). At this static field, the rf frequency coincides with the band minimum ($\omega_{rf} = \omega_{min}$). Rf-power pumps magnons at the band minima, where there is a large amount of available states. Even though they have zero group velocity, sufficient increase of the magnon numbers enhances the overall magnon conductivity [13], giving rise to an enhancement of nonlocal signals.

The three relations discussed above, between the field position of the distinct change of nonlocal resistances and the special position of the dispersion relation with respect to the rf frequency, also apply to 3-GHz and 9-GHz rf frequency and 100-nm YIG cases, which can be found in Ref. [31], S12, and Refs. [33–37,44,45,50–56].

V. CONCLUSION

To conclude, we observe that an rf field can strongly influence magnon spin transport for an in-plane magnetization via kinetic processes and the occupation of relevant magnon states. Firstly, with relatively small rf power, we observe a strong enhancement of the nonlocal signal as large as 800%. It appears only at a positive static field smaller than the FMR condition. This might be a result of effective kinetic processes: the increasing occupation of the magnon band minimum facilitates magnon conduction, and the resulting chiral surface mode manifests itself differently in the positive and negative static fields. Secondly, with large rf power, nonlinear FMR triggers a strong suppression of incoherent thermal magnon transport. This phenomenon is partially due to the heating from microwave power, but the main contribution still remains unclear. We assume that it is related with the scattering between secondary magnons from the NFMR and thermal magnons, which needs more theoretical confirmation. Thirdly, at a static field slightly higher than FMR an enhancement of the thermal magnon transport has been observed, when the rf frequency coincides with the frequency of magnons at the band minima, where the most states are available. This increases the total magnon number resulting in an enhancement of the overall magnon spin conductivity. Therefore our results show that microwave fields can effectively

control thermal magnon spin transport. Moreover, nonlocal magnon spin transport can be used to perform spectroscopy of magnons or spin waves. Our results present a new opportunity to couple electromagnetic signals with spin waves, providing a way to scale down microwave electronics operating at GHz frequencies.

ACKNOWLEDGMENTS

We appreciate G. E. W. Bauer for suggestions and we thank T. Kuschel, T. van der Sar, P. S. Haughian, M. Weiler, A. Kamra, J. Shan, K. Oyanagi, and M. Schabes for discussions. We acknowledge H. M. de Roosz, J. G. Holstein, H. Adema, and T. J. Schouten for their technical assistance. This work is part of the research program Magnon Spintronics (MSP) No. 159 financed by the Netherlands Organisation for Scientific Research (NWO). We appreciate support from the NanoLab NL and the Zernike Institute for Advanced Materials. This research is partly financed by the NWO Spinoza prize awarded to Prof. B. J. van Wees. Further support by EU FP7 ICT Grant No. 612759 InSpin and Marie Curie initial training network Spinograph (607904) is gratefully acknowledged.

[1] L. J. Cornelissen, K. J. H. Peters, G. E. W. Bauer, R. A. Duine, and B. J. van Wees, Phys. Rev. B **94**, 014412 (2016).
[2] K.-i. Uchida, H. Adachi, T. Ota, H. Nakayama, S. Maekawa, and E. Saitoh, Appl. Phys. Lett. **97**, 172505 (2010).
[3] S. S.-L. Zhang and S. Zhang, Phys. Rev. B **86**, 214424 (2012).
[4] S. S.-L. Zhang and S. Zhang, Phys. Rev. Lett. **109**, 096603 (2012).
[5] L. J. Cornelissen, J. Liu, R. A. Duine, J. Ben Youssef, and B. J. van Wees, Nat. Phys. **11**, 1022 (2015).
[6] S. T. Goennenwein, R. Schlitz, M. Pernpeintner, K. Ganzhorn, M. Althammer, R. Gross, and H. Huebl, Appl. Phys. Lett. **107**, 172405 (2015).
[7] J. Li, Y. Xu, M. Aldosary, C. Tang, Z. Lin, S. Zhang, R. Lake, and J. Shi, Nat. Commun. **7**, 10858 (2016).
[8] H. Wu, C. H. Wan, X. Zhang, Z. H. Yuan, Q. T. Zhang, J. Y. Qin, H. X. Wei, X. F. Han, and S. Zhang, Phys. Rev. B **93**, 060403(R) (2016).
[9] S. Vélez, A. Bedoya-Pinto, W. Yan, L. E. Hueso, and F. Casanova, Phys. Rev. B **94**, 174405 (2016).
[10] J. Shan, P. Bougiatioti, L. Liang, G. Reiss, T. Kuschel, and B. van Wees, Appl. Phys. Lett. **110**, 132406 (2017).
[11] K. Ganzhorn, T. Wimmer, J. Barker, G. E. Bauer, Z. Qiu, E. Saitoh, N. Vlietstra, S. Geprägs, R. Gross, H. Huebl *et al.*, arXiv:1705.02871.
[12] J. Liu, L. J. Cornelissen, J. Shan, T. Kuschel, and B. J. van Wees, Phys. Rev. B **95**, 140402(R) (2017).
[13] L. J. Cornelissen, J. Liu, B. J. van Wees, and R. A. Duine, Phys. Rev. Lett. **120**, 097702 (2018).
[14] K. Ganzhorn, S. Klingler, T. Wimmer, S. Geprägs, R. Gross, H. Huebl, and S. T. Goennenwein, Appl. Phys. Lett. **109**, 022405 (2016).
[15] R. Lebrun, A. Ross, S. Bender, A. Qaiumzadeh, L. Baldrati, J. Cramer, A. Brataas, R. Duine, and M. Kläui, Nature **561**, 222 (2018).
[16] V. Kruglyak, S. Demokritov, and D. Grundler, J. Phys. D **43**, 264001 (2010).
[17] A. Chumak, V. Vasyuchka, A. Serga, and B. Hillebrands, Nat. Phys. **11**, 453 (2015).
[18] A. V. Chumak, A. A. Serga, and B. Hillebrands, Nat. Commun. **5**, 4700 (2014).
[19] C. Kittel, Phys. Rev. **73**, 155 (1948).
[20] C. W. Sandweg, Y. Kajiwara, A. V. Chumak, A. A. Serga, V. I. Vasyuchka, M. B. Jungfleisch, E. Saitoh, and B. Hillebrands, Phys. Rev. Lett. **106**, 216601 (2011).
[21] T. Seifert, S. Jaiswal, J. Barker, I. Razdolski, J. Cramer, O. Gückstock, S. Watanabe, C. Ciccarelli, A. Melnikov, G. Jakob *et al.*, Nat. Commun. **9**, 2899 (2018).
[22] L. Bocklage, Phys. Rev. Lett. **118**, 257202 (2017).
[23] M. Collet, X. De Milly, O. d. Kelly, V. V. Naletov, R. Bernard, P. Bortolotti, J. B. Youssef, V. Demidov, S. Demokritov, J. Prieto *et al.*, Nat. Commun. **7**, 10377 (2016).
[24] B. Kalinikos, M. Kostylev, N. Kozhus, and A. Slavin, J. Phys.: Condens. Matter **2**, 9861 (1990).
[25] J. Barker and G. E. W. Bauer, Phys. Rev. Lett. **117**, 217201 (2016).
[26] B. Flebus, P. Upadhyaya, R. A. Duine, and Y. Tserkovnyak, Phys. Rev. B **94**, 214428 (2016).
[27] V. L'vov, in *Nonlinear Waves 3* (Springer, 1990), pp. 224–239.
[28] N. Thiery, A. Draveny, V. Naletov, L. Vila, J. Attané, C. Beigné, G. de Loubens, M. Viret, N. Beaulieu, J. B. Youssef *et al.*, Phys. Rev. B **97**, 060409 (2018).
[29] C. Du, T. Van der Sar, T. X. Zhou, P. Upadhyaya, F. Casola, H. Zhang, M. C. Onbasli, C. A. Ross, R. L. Walsworth, Y. Tserkovnyak *et al.*, Science **357**, 195 (2017).
[30] S. Demokritov, V. Demidov, O. Dzyapko, G. Melkov, A. Serga, B. Hillebrands, and A. Slavin, Nature **443**, 430 (2006).
[31] See Supplemental Material at http://link.aps.org/supplemental/10.1103/PhysRevB.99.054420 for more detailed information and data supplemental to the main paper, which includes Refs. [50–56].
[32] J. Shan, L. J. Cornelissen, N. Vlietstra, J. Ben Youssef, T. Kuschel, R. A. Duine, and B. J. Van Wees, Phys. Rev. B **94**, 174437 (2016).
[33] R. Iguchi and E. Saitoh, J. Phys. Soc. Jpn. **86**, 011003 (2016).
[34] M. B. Jungfleisch, A. V. Chumak, A. Kehlberger, V. Lauer, D. H. Kim, M. C. Onbasli, C. A. Ross, M. Kläui, and B. Hillebrands, Phys. Rev. B **91**, 134407 (2015).
[35] B. Kalinikos and A. Slavin, J. Phys. C **19**, 7013 (1986).
[36] Y. S. Gui, A. Wirthmann, and C. M. Hu, Phys. Rev. B **80**, 184422 (2009).
[37] Y. S. Gui, A. Wirthmann, N. Mecking, and C.-M. Hu, Phys. Rev. B **80**, 060402(R) (2009).
[38] A. J. E. Kreil, D. A. Bozhko, H. Y. Musiienko-Shmarova, V. I. Vasyuchka, V. S. L'vov, A. Pomyalov, B. Hillebrands, and A. A. Serga, Phys. Rev. Lett. **121**, 077203 (2018).
[39] J. Eshbach and R. Damon, Phys. Rev. **118**, 1208 (1960).
[40] T. An, V. Vasyuchka, K. Uchida, A. Chumak, K. Yamaguchi, K. Harii, J. Ohe, M. Jungfleisch, Y. Kajiwara, H. Adachi *et al.*, Nat. Mater. **12**, 549 (2013).

[41] D. A. Bozhko, A. A. Serga, P. Clausen, V. I. Vasyuchka, F. Heussner, G. A. Melkov, A. Pomyalov, V. S. L'vov, and B. Hillebrands, Nat. Phys. **12**, 1057 (2016).
[42] A. Y. Dobin and R. H. Victora, Phys. Rev. Lett. **90**, 167203 (2003).
[43] P. Anderson and H. Suhl, Phys. Rev. **100**, 1788 (1955).
[44] H. Suhl, Proc. IREE **44**, 1270 (1956).
[45] H. Suhl, J. Phys. Chem. Solids **1**, 209 (1957).
[46] M. Sparks, *Ferromagnetic-Relaxation Theory* (McGraw-Hill, 1964).
[47] A. Lavrinenko, V. L'vov, G. Melkov, and V. Cherepanov, Zh. Eksp. Teor. Fiz **81**, 1022 (1981).
[48] A. D. Boardman and S. A. Nikitov, Phys. Rev. B **38**, 11444 (1988).
[49] M. G. Cottam, *Linear and Nonlinear Spin Waves in Magnetic Films and Superlattices* (World Scientific, 1994), p. 441.
[50] S. S. Kalarickal, P. Krivosik, M. Wu, C. E. Patton, M. L. Schneider, P. Kabos, T. J. Silva, and J. P. Nibarger, J. Appl. Phys. **99**, 093909 (2006).
[51] L. Onsager, Phys. Rev. **37**, 405 (1931).
[52] L. Onsager, Phys. Rev. **38**, 2265 (1931).
[53] P. Jacquod, R. S. Whitney, J. Meair, and M. Büttiker, Phys. Rev. B **86**, 155118 (2012).
[54] R. Camley, Surf. Sci. Rep. **7**, 103 (1987).
[55] Z. Haghshenasfard, H. T. Nguyen, and M. G. Cottam, J. Magn. Magn. Mater. **426**, 380 (2017).
[56] Y. Guan, W. Bailey, E. Vescovo, C.-C. Kao, and D. Arena, J. Magn. Magn. Mater. **312**, 374 (2007).